Extending Predictive Capabilities to Network Models

Pål-Eric Øren, Stig Bakke, and Ole Jakob Arntzen

We reconstruct 3-D sandstone models which give a realistic description of the complex pore space observed in actual sandstones. The reconstructed pore space is transformed into a pore network which is used as input to a two-phase network model. The model simulates primary drainage and water injection based on a physical scenario for wettability changes at the pore level. We derive general relationships between pore structure, wettability, and capillary pressure for the different pore level displacement mechanisms which may occur in the network model.

We present predicted transport properties for three different reconstructed sandstones of increasing complexity: Fontainebleau, a water wet Bentheimer, and a mixed wet reservoir rock. Predicted transport properties are in good agreement with available experimental data. For the reservoir rock, both the experiments and the simulated results show that continuos oil films allow low oil saturations to be reached during forced water injection. However, the oil relative permeability is very low.

Introduction

The microstructure of a porous medium and the physical characteristics of the solid and the fluids which occupy the pore space determine several macroscopic properties of the medium. These properties include transport properties of interest such as permeability, formation factor, relative permeability, and capillary pressure. In principle, it should be possible to determine these properties by appropriately averaging the equations describing the physical processes occurring on the pore-scale. The prediction of macroscopic transport properties from the associated pore-scale parameters is a long-standing issue which has been the subject of much investigation. One commonly applied tool in this investigation is the network model.

The premise of the network model is that the void space of a porous medium can be represented by a network of interconnected pores in which larger pores (pore bodies) are connected by smaller pores (pore throats). Since the pioneering work of Fatt[1-3], network models have been used extensively to study different displacement processes in simple or idealised porous media[4-20]. Seldom, however, do such models claim to be representative of reservoir rocks[21].

The extension of network modeling techniques to real porous media is hampered by the difficulty of adequately describing the complex nature of the pore space. Advanced techniques such as microtomographic imaging[21-25] and serial sectioning[26-27] provide a detailed description of the pore space at micrometer resolution. In practice, however, information about the microstructure of reservoir rocks is limited to 2-D thin section images and to pore throat entry sizes determined from mercury injection. These data are insufficient to directly construct a 3-D pore network which replicates the microstructure of the medium. As a result, simplifying assumptions about the topology and geometry of the pore structure must be invoked.

Despite these simplifications, network models have proved to be powerful tools for extrapolating limited measured data and for developing valuable insight into complex multiphase flow phenomena such as capillary pressure and relative permeability hysteresis[12,28], the effect of wettability[29-32], and three-phase flow[33-38]. However, the difficulty in adequately describing the pore network of reservoir rocks has prevented network models from being used as a predictive tool, thus greatly limiting their application in the oil industry.

In the present work, geostatistical information obtained from image analyses of 2-D thin sections are used to generate a reliable reconstruction of the complex rock-pore system in 3-D. The network representation of the pore space is constructed from topological and geometrical analyses of the fully characterised reconstructed sample. The pore network is used as input to a two-phase network model which simulates drainage and water injection based on a physical model for wettability alteration on the pore level. Predicted transport properties for different reconstructed sandstones are compared with experimental data.

Paper first presented at the SPE Annual Technical Conference & Exhibition held in San Antonio, U.S.A., 5-8 October, 1997.

Received for review, November 23, 1995
Revised, April 1, 1996
Accepted for publication, June 15, 1996
Camera-ready copy received, October 14, 1996

Experimental

The experimental measurements reported here were performed on outcrop and on reservoir sandstones. The outcrop rock consisted of three homogenous core samples which were cut from a single block of Bentheimer quarried sandstone. This strongly water wet sandstone is well-sorted and composed mainly of quartz (70-80%), feldspar (20-25%), and authigenic clays (2-3%). The main clay component is pore-filling kaolinite. The reservoir rock consisted of two preserved mixed wet core plugs. This North Sea Lower Brent reservoir rock is a micaceous (10-12%) feltspatic (15-19%) sandstone with abundant pore-filling kaolinite. Petrophysical properties for the different plug samples are given in **Table 1**.

The Bentheimer plugs were tested at room temperature using synthetic brine (3% NaCl) and a paraffinic oil. Measurements on the reservoir core plugs were performed at 70°C using simulated formation brine and a dead crude oil. Fluid properties at the specific test conditions are summarised in **Table 2**.

TABLE 1—PETROPHYSICAL PROPERTIES FOR BENTHEIMER (B) AND RESERVOIR ROCK (R) SAMPLES

Sample	Porosity	ρ (g/cm^3)	k_w (mD)	FRF
B1	0.232	2.640	2840	11.6
B2	0.241	2.650	2820	12.1
B3	0.237	2.647	2930	12.0
R1	0.297	2.67	358	
R2	0.293	2.67	326	

TABLE 2—TEST CONDITIONS AND FLUID PROPERTIES

Property	Bentheimer	Reservoir Rock
temperature	20 °C	70°C
brine density	1.02 g/cm^3	0.99 g/cm^3
brine viscosity	1.06 cp	0.43 cp
oil density	0.76 g/cm^3	0.83 g/cm^3
oil viscosity	1.40 cp	3.11 cp
oil-water IFT	35.0 mN/m	7.1 mN/m

Capillary Pressure. Primary drainage capillary pressure functions for the Bentheimer core plugs were measured by the porous plate method. A ceramic porous plate with a gas-water threshold pressure of 15 bar was installed on the lower end-face of the vertically oriented sample. Water production was measured at nine different drainage pressures in the range zero to 5 bar. The measured capillary pressure data were similar for all three samples and are summarised in **Table 3**.

Waterflood and secondary drainage capillary pressure functions for the reservoir core plugs were determined from centrifuge displacements. Fluid saturations were calculated from material balance and Karl Fischer analysis at the end of the experiments. The capillary pressure data for the two samples were similar and are tabulated in **Table 4**. Spontaneous imbibition of water (oil) were measured prior to the waterflood (secondary drainage) and used to calculate Amott wettability indices. Both core plugs spontaneously imbibed both water and oil and the Amott wettability indices (0.08 and 0.1) indicate that the samples are mixed wet.

TABLE 3—PRIMARY DRAINAGE CAPILLARY PRESSURE DATA FOR THE BENTHEIMER SAMPLES

	Water Saturation		
Pc (kPa)	Sample B1	Sample B2	Sample B3
0	1.0	1.0	1.0
2.5	1.0	0.972	0.956
5.0	0.692	0.648	0.423
10.0	0.135	0.137	0.129
20.0	0.090	0.098	0.093
40.0	0.073	0.080	0.079
80.0	0.063	0.068	0.068
150.0	0.056	0.062	0.063
300.0	0.054	0.057	0.058
500.0	0.051	0.052	0.055

TABLE 4—CAPILLARY PRESSURE DATA FOR THE RESERVOIR ROCK SAMPLES

Forced Water Injection			Secondary Drainage		
Pc (kPa)	Sw (R1)	Sw (R2)	Pc (kPa)	Sw (R1)	Sw (R2)
0.0	0.403	0.441	0.0	0.774	0.771
-1.8	0.688	0.711	0.9	0.610	0.608
-4.1	0.763	0.771	2.1	0.343	0.349
-7.3	0.802	0.817	4.7	0.232	0.241
-13.8	0.820	0.840	11.4	0.208	0.202
-32.9	0.876	0.890	33.5	0.176	0.193
-71.1	0.901	0.936	75.3	0.172	0.189
-139.5	0.918	0.936	145.2	0.167	0.188
-278.9	0.950	0.950	284.8	0.162	0.188

Relative Permeability. Primary drainage and waterflood relative permeability curves for the Bentheimer plugs were determined by the steady state method. The measurements were performed on vertically oriented samples. The total flowrate (200 cm^3/hr) was constant during the experiments. Steady state relative permeability measurements were obtained by keeping the oil and water flowrates constant until the conditions in the core stabilised. The pressure drop across the core was monitored continuously using a differential pressure transducer. Relative permeability to each phase was calculated using Darcy's law.

Oil relative permeabilities for the reservoir rock during forced water injection (*i.e.*, negative capillary pressure) were determined from a single speed (2500 RPM = -70kPa) centrifuge displacement applying Hagoort's analytical method[39] to compute relative permeability. Fluid production was monitored using an automated centrifuge system (CENTAS). Production data were recorded every two seconds at the beginning of the displacement and then at increasing intervals up to every five minutes. The experiment run for 14 hours.

Thin Section Analysis. Thin sections were prepared from the end pieces of the core plugs used in the experiments. Back-scattered SEM (BSE) images of the thin sections were binarised and analysed using a KONTRON KS400 image

analyser. An erosion-dilation algorithm was used to partition the sandgrain matrix into discrete grains. We measured the diameter of each grain and constructed a grain-size distribution curve. Cathodoluminescence images were used to distinguish quartz cement from the original detrital grains.

The measured grain diameter is correct only if the thin section cuts through the centre of the grain. The ratio of the measured grain diameter to the quartz cement thickness was used to determine whether or not the section cuts close to the grain centre. If this ratio is below a pre-defined cut-off value, which depends on the degree of quartz cementation, the grain diameter is assumed to be non-representative and the grain is removed from the grain-size distribution curve.

The porosity of the sample is defined as the fraction pore area contained in the BSE image. It is determined by first thresholding the epoxy-filled pore space from the rock matrix and then measure the corresponding area. The total amount of clay is determined similarly. The BSE-signals from clays fall in-between the epoxy and quartz/feldspar signals. By thresholding the clay one may thus measure the total amount of clay in the image. The clay texture is determined visually.

Sandstone Reconstruction

The results from the thin section analyses are used to reconstruct 3-D sandstone models. The reconstruction algorithm has been described in detail previously[40]. The essence of our approach is to build sandstone models which are analogs of actual sandstones by stochastically model the results of the main sandstone forming processes - sedimentation, compaction, and diagenesis. In the present work, the modeling of the sedimentation and compaction processes are identical to that described previously[40]. The diagenesis modeling has been extended to include non-uniform quartz cement overgrowth and microporous pore-lining and pore-filling clays or cements.

In our initial attempt[40] at modeling quartz cement overgrowth, the radii of all the sandgrains were increased uniformly. As shown by Schwartz and Kimminau[41], more realistic algorithms can be defined by letting the rate of cement growth depend on the direction of growth. For each direction **r** (measured from the grain centre), we define the length $l(\mathbf{r})$ as the distance between the surface of the original spherical grain and the surface of its Voronoi polyhedron[40,42]. The rate of increase of the distance $L(\mathbf{r})$ between the grain centre and the pore-grain surface is controlled by a cement growth exponent α according to the formula[41]

$$L(\mathbf{r}) = R_o + \min(al^{\alpha}, l) \qquad (1)$$

where R_o is the radius of the original spherical grain and a simply controls the amount of cement growth (*i.e.*, the porosity). The effect of the growth exponent α is illustrated in **Fig. 1**. Positive values of α favour growth of cement in the directions of large $l(\mathbf{r})$ (*i.e.*, the pore bodies). There is a

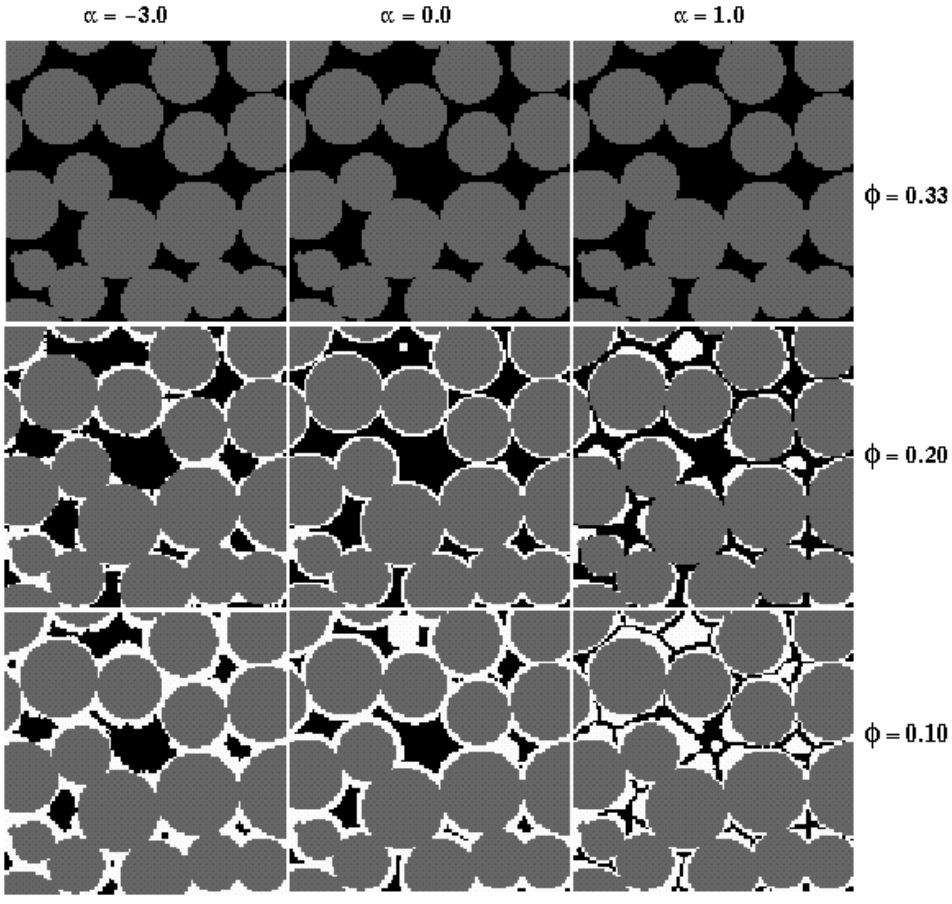

Fig.1—Cross-sections of computer generated models illustrating the effect of increasing volumes of quartz cement overgrowth for negative (left) and positive (right) values of the cement growth exponent.

clear tendency to form sheet-like pores as the porosity decreases. This ensures that the pore space remains interconnected down to very low porosities. Negative values of α favour growth toward the directions with the smallest $l(\mathbf{r})$ (*i.e.*, the pore throats). Pore throats thus tend to be closed off as the porosity decreases. This increases the tortuosity of the medium and the porosity (*i.e.*, threshold percolation porosity) at which the connectivity of the pore space vanishes is higher than that for $\alpha > 0$. If $\alpha = 0$, quartz cement deposits as concentric overgrowth on the grains.

Many varieties of clays or cements may precipitate in the pore space during the diagenetic stages. Diagenetic clays clog and sub-divide pore space and generate microporosity. Pores within the microporosity are typically one or two orders of magnitude less than the intergranular pores. We assume that the permeability of these pores is negligible compared to that of the intergranular pore space.

The morphology of the common diagenetic clays can be divided into three broad categories: pore-lining, pore-filling, and pore-bridging. Pore lining clays typically form thin crystals which grow radially outward from the surface of the detrital grains. Typical examples are chlorite, illite, and smectite. Pore-lining clays are modeled by randomly precipitating clay particles (voxels) on the surfaces of the detrital grains or the quartz cement. **Fig. 2** shows that the presence of pore-lining clays reduces the size of the intergranular pores. However, their effect on altering the effective tortuosity of the medium is small.

Pore-filling clays such as pseudo-hexagonal booklets of kaolinite are modeled using a clay clustering routine which causes clay particles (voxels) to precipitate preferentially in randomly selected pore bodies. **Fig. 2** shows that pore-filling clays tend to form tight clusters of particles which clog or block off pore throats even at relatively high porosities. The presence of pore-filling clays thus increases the tortuosity of the medium significantly.

The morphology of the clay and the total amount of clay to be precipitated in our models are determined from petrographical analyses of thin sections. Pore-bridging clays are currently not implemented.

Pore Network. An example of a reconstructed pore space is shown in **Fig. 3**. Although it is possible to perform flow simulations directly on the chaotic pore space, either by numerically solving the Navier Stokes equation[43,44] or by applying a Lattice Boltzmann simulation[45], it can only be done at considerable computational expense. It is therefore convenient to construct a pore network which replicates the essential features of the pore space that are relevant to fluid flow. The transformation of the reconstructed pore space into a pore network and the topological and geometrical characterisation of the network has been described in detail previously[40].

Pore Shape. A key characteristic of real porous media is the angular corners of pores. Angular corners retain wetting fluid and allow two or more fluids to flow simultaneously

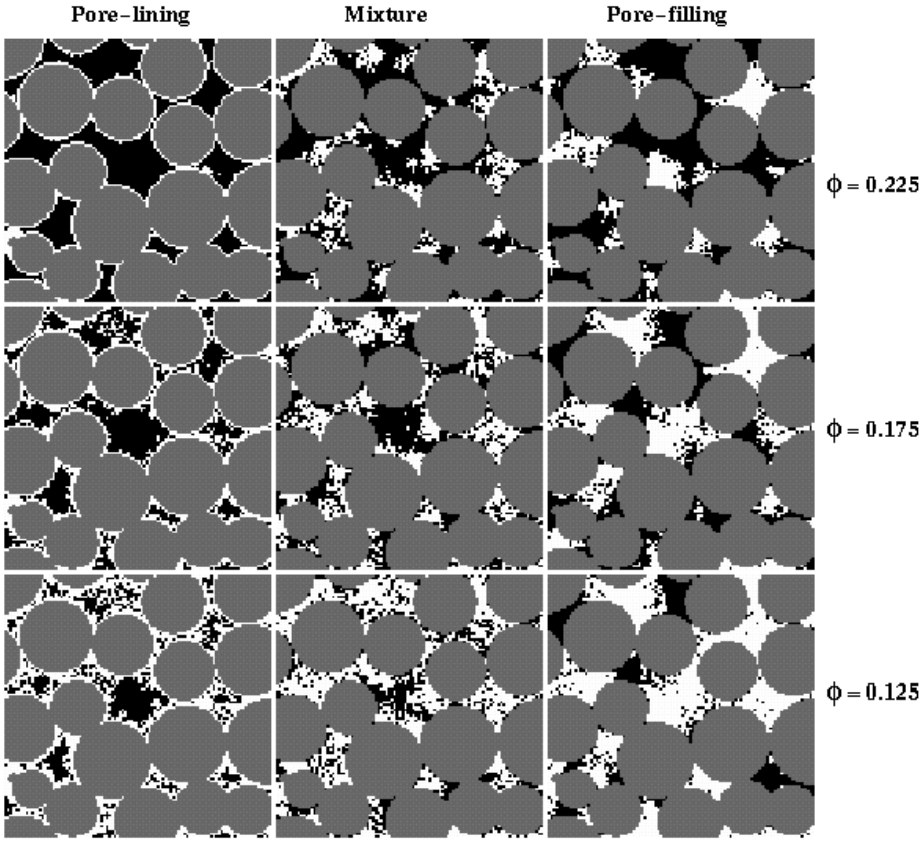

Fig.2—Cross-sections of computer generated models illustrating the effect of increasing volumes of pore-lining (left) and pore-filling (right) clays.

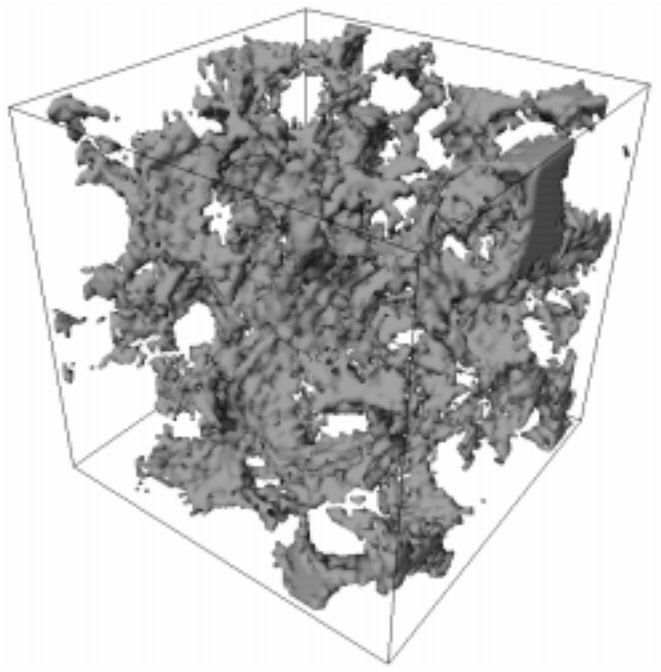

Fig. 3—A small cube of a reconstructed pore space. The linear scale of the model is 100 voxels (0.75mm) on each side.

through the same pore. Pores which are angular in cross-section are thus a much more realistic model of the pore structure than the commonly applied cylindrical shape. In the present work, the shape of every pore body and throat is described in terms of a dimensionless shape factor G which is defined as[46]

$$G = \frac{\overline{A}}{s^2} \tag{2}$$

where $\overline{A}$ is the average cross-sectional area of the pore body or throat and s is the corresponding perimeter length. The area and perimeter length are determined by standard image analysis techniques. The shape factor replaces the irregular shape of a pore body or throat by an equivalent irregular triangular shape. It ranges from zero for a slit shaped pore to 0.048 for an equilateral triangular pore.

It is useful to relate G to the actual shape of the pore body or throat. From elementary geometry, G may be expressed as

$$G = \frac{1}{4}\left(\sum_{i=1}^{3}\frac{1}{\tan\beta_i}\right)^{-1} \tag{3}$$

where β is the corner half angle ($\beta_1 \le \beta_2 \le \beta_3$). Obviously, a single value of G corresponds to a range of shapes. The combinations of β_1 and β_2 which give a constant G is[46]

$$G = \frac{\sin(2\beta_1)}{2}\left(2 + \frac{\sin(2\beta_1)}{\sin(2\beta_2)}\right)^{-2} \tag{4}$$

For a given G, the minimum and maximum allowed values of β_2 are found from Eq. (4) by setting $\beta_2 = \beta_1$ and $\beta_2 = \pi/4 - \beta_1/2$, respectively. In the present work, corner angles are assigned to pore bodies and throats by first randomly selecting β_2 ($\beta_{2,\min} \le \beta_2 \le \beta_{2,\max}$). The remaining angles may then be determined from Eq. (3).

Flow in the Network

We wish to simulate two-phase flow in our pore networks. The displacing fluid is injected through an external reservoir which is connected by pore throats to every pore body on the inlet side of the network. The displaced fluid escapes through the outlet face on the opposite side. Periodical boundary conditions are imposed along the sides parallel to the main direction of flow.

We assume that capillary forces dominate at the pore-scale. This is a reasonable assumption for low capillary number (10^{-6} or less) processes[47] which are typical of most reservoir displacements. In the following, we present a precise description of the different pore-scale displacement mechanisms which may occur in the pore network during primary drainage and water injection.

Primary Drainage. Initially, the network is fully saturated with water and is strongly water wet. Oil then enters the network representing migration into the reservoir. At every stage of the process, oil invades the available pore body or throat with the lowest threshold capillary pressure. This forms the basis for the invasion percolation algorithm[48,49] used previously to model drainage processes.

Threshold or entry capillary pressures are calculated using the Mayer & Stowe[50] and Princen[51-53] (MS-P) method. The details of the calculations are given in Appendix A. The threshold capillary pressure is governed by both the pore shape and the receding contact angle θ_r

$$P_c^e = \frac{\gamma(1+2\sqrt{\pi G})\cos\theta_r}{r} F_d(\theta_r, G) \tag{5}$$

where r is the inscribed radius of the pore body or throat. In general, the function F_d is dependent on the particular corner angles and is thus not universal for a specific G. In practice, however, F_d varies little for a given G. This is illustrated in **Fig. 4** which shows the full variation in F_d when water is present in at least one of the corners. For strongly water wet systems (*i.e.*, $\theta_r = 0^o$), $F_d = 1$.

Wettability Alteration. When oil initially invades a water filled pore body or throat, a stable water film protects the pore surface from wettability change by adsorption. At a critical capillary pressure, the film collapses to form a molecular thin film. This allows surface active components in the oil to adsorb on the pore surface. The capillary pressure at which the water film ruptures depends on the curvature of the pore wall and on the shape of the disjoining pressure isotherm. Kovscek *et al.*[54] present a detailed analysis of this scenario for star-shaped pores. Blunt[32] recently extended the analysis to square pores and presents a parametric model for the critical capillary pressure at which the water film collapses. A similar approach is adopted here.

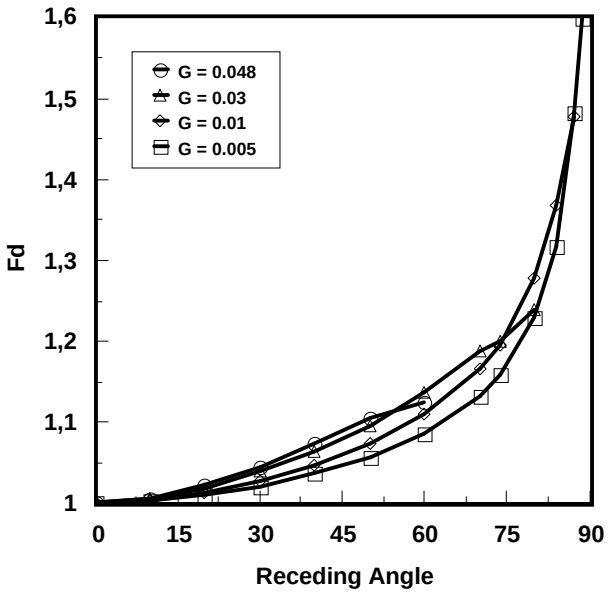

Fig. 4—$F_d(\theta_r,G)$ vs. θ_r when water is present in at least one of the corners. The results for each G are the average of 1000 realisations.

For a pore body or throat *i*, the critical capillary pressure P_c^* is given by

$$P_{c,i}^* = \Pi_i + \Gamma_i x_i \qquad (6)$$

where Π and Γ are input parameters and x varies uniformly between zero and one. The first term on the right represents the disjoining pressure whilst the second term represents the film curvature. If P_c^* is exceeded in an oil filled pore body or throat, the contact angle must change[54]. We assume that the new value of θ_r < 90° - β_1. This ensures that water is always present in at least one of the corners.

Primary drainage and the film rupturing process continues until a maximum capillary pressure $P_{c,\max}$ is reached. If $P_{c,\max}$ exceeds P_c^* in a pore body or throat, the water film collapses and the wettability changes. In this case, the corners contain bulk water and remain water wet. Away from the corners, adsorption of hydrophobic components make the pore wall oil wet. We refer to these pore bodies and throats as being mixed wet. Pore bodies and throats where $P_{c,\max} < P_c^*$ remain water wet.

Water Injection. The capillary pressure drops during water injection and water first invades the available water wet pore bodies and throats. Pore-scale displacement mechanisms for strongly wetting systems have been described by Lenormand *et al.*[55]. There are three types of displacements: *piston type*, *pore body filling*, and *snap-off*. Below we summarise the behaviour and the threshold capillary pressures for each of these displacement in mixed wet pores.

Piston Type. This refers to the displacement of oil from a pore throat by an invading interface initially located in an adjoining water filled pore body. If there is no contact angle hysteresis, the threshold capillary pressure is the same as for drainage (Eq. (5)). In a more realistic scenario, the advancing contact angle θ_a is different from θ_r. This is always true for mixed wet systems where θ_a may be much larger than θ_r.

In this case, there is a range of capillary pressure where the invading interface remains pinned. As the capillary pressure drops, the interface remains fixed in place and the contact angle adjusts to a new value θ_h. The hinging angle θ_h can acquire any value between θ_r and θ_a. Water enters the throat once the capillary pressure is lowered sufficiently that θ_a is reached. The calculation of the threshold capillary pressure for this case is given in Appendix A.

Solutions for the normalised threshold capillary pressure ($P_c^N = rP_c^e/\gamma$) shows that spontaneous imbibition ($P_c^N > 0$) by piston type displacement always occurs for θ_a less than 90° and may occur for θ_a much greater than 90° (**Fig. 5)**. The maximum advancing angle at which spontaneous imbibition occurs is given by

$$\theta_{a,\max} = \cos^{-1}\left[\frac{-4G\sum\cos(\theta_r + \beta_i)}{P_c^{Nd} - \cos\theta_r + 12G\sin\theta_r}\right] \qquad (7)$$

where $P_c^{Nd} = rP_{c,\max}/\gamma$. The maximum advancing angle for spontaneous imbibition thus depends on $P_{c,max}$, G, and θ_r which, in turn, determines the residual water saturation in oil invaded pores. This is illustrated in **Fig 6** which shows that $\theta_{a,\max}$ and therefore spontaneous imbibition decreases when the residual water saturation is reduced.

If the advancing angle is greater than $\theta_{a,\max}$, the water invasion is forced. Forced water invasion is analogous to the oil drainage process. If θ_a > 90° + β_1, the entry capillary pressure may be determined from Eq. (5). If θ_a < 90 ° + β_1, the threshold capillary pressure is given by

$$P_c^e = \frac{2\gamma\cos\theta_a}{r} \qquad (8)$$

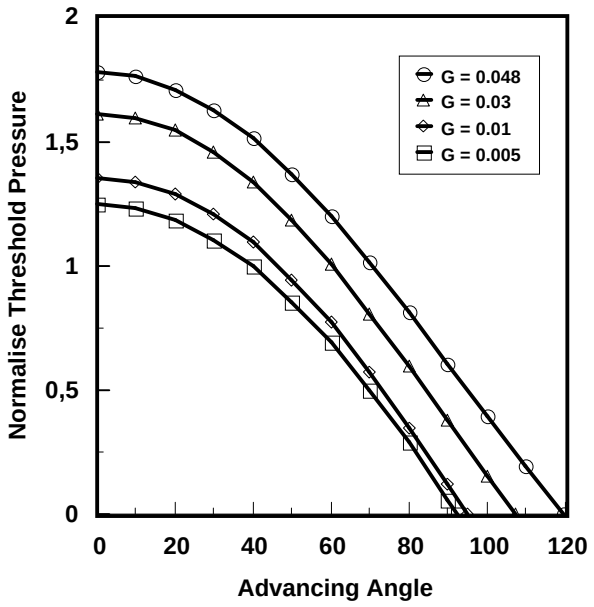

Fig. 5—Normalised threshold pressure for piston displacement. The receding angle is zero and P_c^{Nd} = 2.

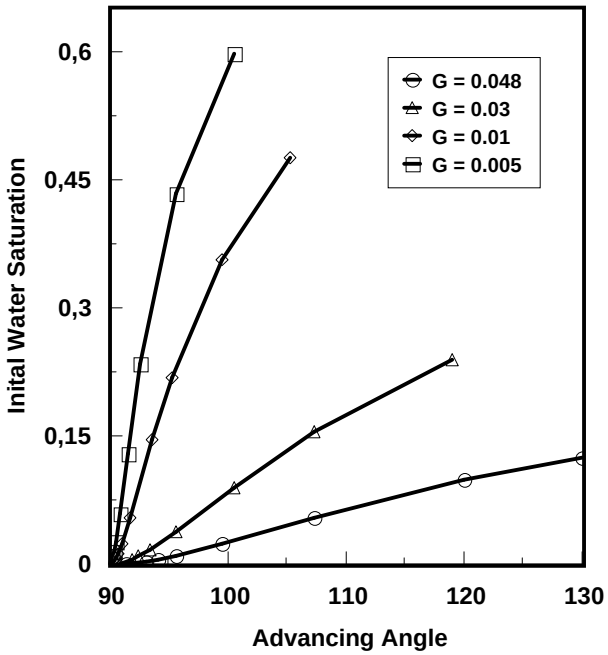

Fig. 6—Effect of initial water saturation on the maximum contact angle at which spontaneous imbibition by piston type displacement occurs. The receding angle is zero.

Pore body filling. The threshold capillary pressure for pore body filling is limited by the largest radius of curvature required to invade the pore body. This radius depends on the size of the pore body and on the numbers of connecting throats filled with oil. For a pore body with coordination number z, there are z-1 such mechanisms, referred to as I_1 to I_{z-1}. If only one of the connecting throats contain oil (*i.e.*, I_1), the filling of the pore body is similar to that of a piston type invasion and the threshold capillary pressure is the same as for the corresponding piston type displacement.

The threshold capillary pressures for the I_2 to I_{z-1} mechanisms are more complex, especially for the chaotic networks used in the present work. Blunt[32] presents a parametric model for this and a similar approach is used here. If $\theta_a < \theta_{a,\max}$, the mean radius of curvature for filling by an I_n mechanism is computed as

$$R_n = \frac{1}{\cos\theta_a}\left(r_p + \sum_{i=1}^{n} b_i r_i x_i \right) \qquad (9)$$

where r_p is the pore body radius, b_i are input parameters, r_i are the radii of the oil filled throats, and x_i are random numbers between zero and one. The threshold capillary pressure is $P_{c,n} = 2\gamma/R_n$. If $\theta_a > \theta_{a,\max}$, the water invasion is forced and the threshold capillary pressure is the same as for the I_1 mechanism.

Snap-Off. Snap-off refers to the invasion of an oil filled pore space by arc menisci (AMs) which always exist in the corners of oil filled pore bodies and throats. In the absence of contact angle hysteresis, the AMs advance smoothly along the pore walls as the capillary pressure drops. At a critical point, the AMs fuse together and the centre of the pore space spontaneously fills with water. For a strongly water wet system, this occurs at a threshold capillary pressure $P_c^e = \gamma/r$.

If there is contact angle hysteresis, the AMs remain pinned at the position established at $P_{c,\max}$ until the hinging angle in the sharpest corner equals θ_a. Further decrease in the capillary pressure causes the AM to advance towards the centre of the pore space. Eventually, this AM meets another AM, causing snap-off. If $\theta_a < 90^o - \beta_1$, the curvatures of the AMs are positive and snap-off occurs at a positive capillary pressure. The capillary pressure at which this occurs can be calculated from elementary geometry (Appendix A). In contrast to piston type invasion, spontaneous imbibition by snap-off only occurs for $\theta_a < 90^o$ (**Fig. 7)**.

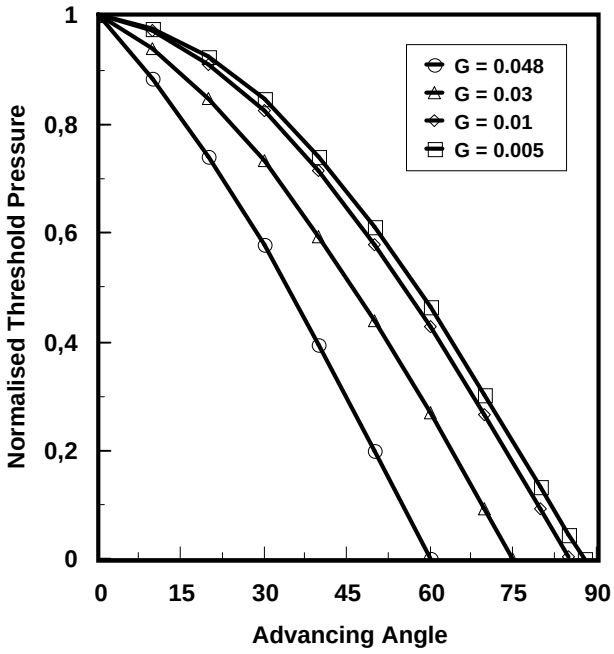

Fig. 7— Normalised threshold pressure for snap-off. The receding angle is zero and $P_c^{Nd} = 2$. The results for each G are the average of 1000 realisations.

If $\theta_a > 90^o - \beta_1$, the curvatures of the AMs are negative and the invasion is forced. Once the hinging angle in the sharpest corner has increased to θ_a, the AM advances towards the centre of the pore space. This causes the absolute value of the negative curvature to decrease. The AM is thus unstable and the pore body or throat immediately fills with water. The threshold capillary pressure for this process depends on the curvature of the AM when it begins to move. It is given by

$$P_c^e = P_{c,\max}\frac{\cos(\theta_a + \beta_1)}{\cos(\theta_r + \beta_1)} \qquad \theta_a \le 180^o - \beta_1 \qquad (10)$$

$$P_c^e = P_{c,\max}\frac{-1}{\cos(\theta_r + \beta_1)} \qquad \theta_a \ge 180^o - \beta_1 \qquad (11)$$

Formation of Oil Films. Piston like advance in a mixed wet pore body or throat leaves the centre of the pore space filled with water. If $\theta_a > 90^o + \beta_1 > \theta_{a,\max}$, a film of oil may be left sandwiched in between the water in the corner(s) and

the water in the centre. These films may significantly increase the connectivity of the oil phase and allow oil mobility down to very low saturations.

Similar to Blunt[32], we assume that the oil film in a corner is stable until the two oil-water interfaces on either side of the film meet. The critical capillary pressure at which an oil film in a corner *i* collapses is thus given by

$$\frac{P_c}{-P_{c,\max}} = \frac{\sin\beta_i}{\cos(\theta_r + \beta_i)}\left(\frac{1-d^2}{d\cos\beta_i + \sqrt{1-d^2\sin^2\beta_i}}\right) \quad (12)$$

where $d = 2 + \cos\theta_a/\sin\beta_i$.

Fluid Volumes and Conductances

Pore bodies and throats are assumed to have a triangular cross-section with area $A = r^2/4G$. When water is present as AMs in the corners of a pore body or throat, the area occupied by the water is given by

$$A_w = r_w^2 \sum_{i=1}^{3}\left[\frac{\cos\theta\cos(\theta+\beta_i)}{\sin\beta_i} - \frac{\pi}{2}\left(1 - \frac{\theta+\beta_i}{90}\right)\right] \quad (13)$$

where $r_w = \gamma/P_c$ is the radius of curvature of the AMs and θ can be θ_r, θ_h, or θ_a depending on the circumstances. When oil films are present in the corners of a pore body or throat, the area occupied by the oil is

$$A_o = r_w^2 \sum_{i=1}^{3}\left[\frac{\cos\theta_a\cos(\theta_a-\beta_i)}{\sin\beta_i} - \frac{\pi}{2}\left(\frac{\theta_a-\beta_i}{90} - 1\right)\right] - A_w \quad (14)$$

where A_w is given by Eq. (13) and the sum only includes the corners where oil films exist. The volume of water or oil is assumed to be the fraction of the cross-section occupied by the phase multiplied by the total pore body or throat volume. The volume of trapped fluid is computed using the capillary pressure at which the fluid was first trapped. The overall saturation of each phase is found by adding the volume of each phase in every pore body and throat and dividing by the total pore volume of the network.

Conductances. The hydraulic conductance of completely filled pore bodies and throats is computed by assuming a Poiseuille law relation between the flow rate q and the pressure gradient ∇P

$$q = -g\nabla P \quad (15)$$

At low Reynolds numbers, incompressible flow in a straight horizontal pore body or throat may be described in dimensionless form as

$$\frac{\partial^2 u}{\partial Y^2} + \frac{\partial^2 u}{\partial Z^2} = -1 \quad (16)$$

where the independent space variables $y = Y\sqrt{A}$ and $z = Z\sqrt{A}$. The dimensionless velocity u is defined as

$$u = \frac{v_x\mu}{A(-dP/dx)} \quad (17)$$

The boundary condition is that u=0 along the walls of the pore body or throat. Eq. (16) was solved using a standard finite difference method. Hydraulic conductances were determined by integrating the computed velocity field over the pore body or throat cross-section.

Computed conductances for different shaped triangular pores are shown in **Fig. 8**. The functional dependency between g and the shape factor G is almost linear and is closely approximated by

$$g = \frac{3A^2G}{5\mu} = \frac{3r^2A}{20\mu} \quad (18)$$

If oil occupies the centre of a pore body or throat with water present as AMs in the corners, the oil conductance is found from Eq. (18), but with A replaced by the cross-sectional area occupied by oil.

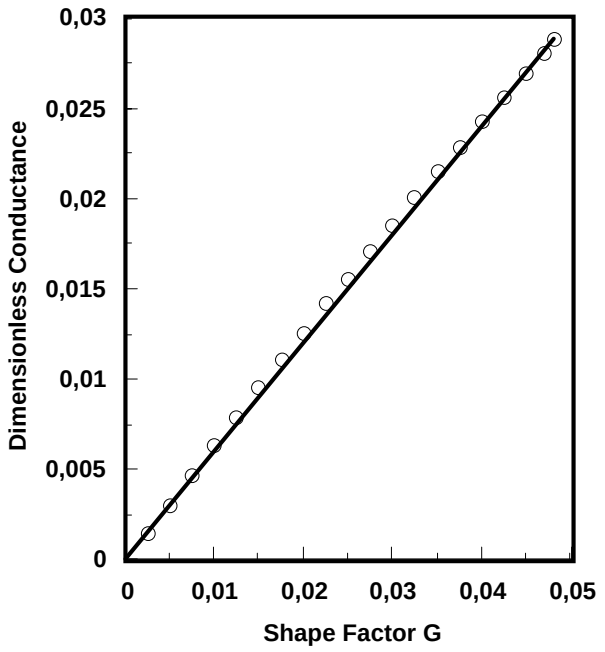

Fig. 8—Computed dimensionless conductances ($g\mu/A^2$) as a function of the shape factor for different triangular shaped pores.

When water is present as AM in a corner i with a contact angle less than $90^o - \beta_i$, the water conductance is

$$g_{w,i} = \frac{r_w^2 A_{w,i}}{C_{w,i}\mu} \quad (19)$$

where C_w is a dimensionless flow resistance factor which accounts for the reduced water conductivity close to the pore walls. Numerical solutions of the corner flow problem[56] show that C_w depends on the corner geometry, the contact

angle, and the boundary condition at the oil-water interface. The total conductance is the sum of all the corner conductances.

If the contact angle is greater than 90^o - β_i, the curvature of the AM is negative and we do not have an exact expression for the conductance. In this case, we use an approximation based on Eq. (19) which may be written as

$$g_{w,i} = \frac{A_{w,i}^2}{C_{w,i}\kappa_i \mu} \tag{20}$$

where C_w is evaluated at $\theta = 0^o$ and κ is given by

$$\kappa_i = \frac{\cos\beta_i}{\sin\beta_i} - \frac{\pi}{2}\left(1 - \frac{\beta_i}{90}\right) \tag{21}$$

If oil films are present in the corners of a pore body or throat, the oil conductance is found from Eq. (20) but with A_w replaced by A_o . This is an approximation since the geometry of the oil film is different to that of a water AM[32].

Macroscopic Properties. For laminar flow, the flow rate of fluid *i* between two connecting nodes *I* and *J* is given by

$$q_{i,IJ} = \frac{g_{i,IJ}}{L_{IJ}}(P_{i,I} - P_{i,J}) \tag{22}$$

where L_{IJ} is the spacing between the pore body centres. The effective conductance $g_{i,IJ}$ is assumed to be the harmonic mean of the conductances of the throat and the two pore bodies themselves, *i.e.*,

$$\frac{L_{IJ}}{g_{i,IJ}} = \frac{L_t}{g_{i,t}} + \frac{1}{2}\left(\frac{L_I}{g_{i,I}} + \frac{L_J}{g_{i,J}}\right) \tag{23}$$

where the subscript *t* denotes the pore throat. We impose mass conservation at each pore body, which means that

$$\sum_J q_{i,IJ} = 0 \tag{24}$$

where *J* runs over all the pore throats which are connected to pore body *I*. Eqs. (22-24) give rise to a set of linear equations for the pore body pressures.

The permeability of the network is computed by imposing a constant pressure gradient across the network and let the system relax using a conjugate gradient method to determine the pore body pressures. From the pressure distribution we calculate the total flow rate and thus the permeability using Darcy's law. Relative permeabilities are computed similarly. At various stages of the displacement, we compute the pressure drop in each phase separately. The saturation and the total flow rate in each phase are also calculated. Relative permeabilities may then be determined from Darcy's law.

Because of the analogy between Poseuille's law and Ohm's law, the flow of electrical current in the network is also described by Eqs. (22-24), but with pressure replaced by voltage and hydraulic conductance by electrical conductance. The electrical conductance g_e is assumed to depend only upon the geometry of the pore body or throat (*i.e.*, pore walls are insulating) and is given by

$$g_e = \sigma_w A \tag{25}$$

where σ_w is the electrical conductivity of the fluid which fills the pore network. The electrical conductivity σ of the pore network is computed by applying a constant voltage drop across the network and then use Eq. (22) to find the flow of current between each pore body. From this one may calculate the total current and thus the formation factor, *FRF* = σ_w/σ.

Results

Fontainebleau sandstone. The sandstone reconstruction algorithm was validated by comparing a reconstructed sample of Fontainebleau sandstone with microtomographic images of the actual sample. **Fig. 9** compares the standard deviation in local porosity for the two samples. Local porosity distributions were measured using a moving box technique with a logarithmic increase in box size. This ensures that both local and global variations in porosity are captured. The model closely mimics the actual sample, except at large box sizes where the variation in porosity is too small. This suggests that the reconstructed model does not capture all of the global heterogeneities which are present in the real sample.

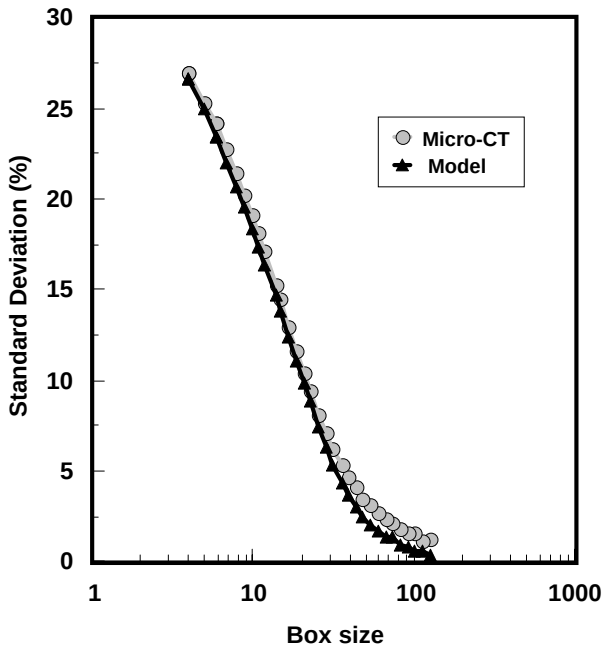

Fig. 9—Standard deviation in local porosity for a reconstructed model and a micro-CT image of a Fontainebleau sandstone.

The horizontal and vertical two-point correlation functions were computed as a function of varying box size and distance, thus covering both local and global correlations. These correlation functions may be represented as 2-D surfaces and are shown in **Fig. 10**. The correlation functions for the two samples are very similar. Statistical analysis (ANOVA) shows that there is no significant differences within the level of noise we experience (1000 replications for each box size-distance combination).

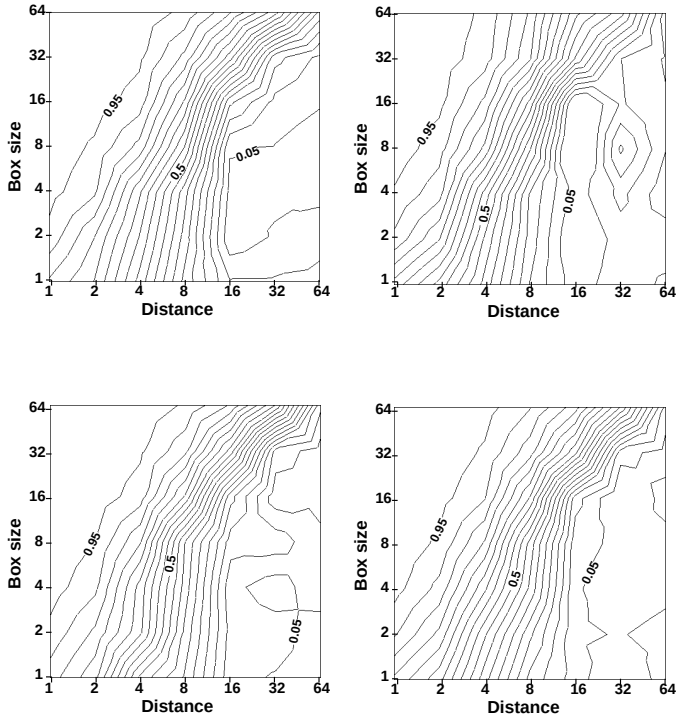

Fig. 10—Horizontal (top) and vertical (bottom) two-point correlation functions for the Fontainebleau sandstone. Micro-CT image to the left, reconstructed model to the right (1 unit = 7.5 μm).

Bourbie and Zinszer[57] performed extensive laboratory measurements of the hydraulic properties of Fontainebleau sandstone. The Fontainebleau sandstone is an aeolan fine grained quartzite. Thin section analyses reveal that it is well sorted with an average grain size of around 200μm. The porosity and permeability, however, vary widely. The variation in these properties is predominantly due to variation in the volume of quartz cement overgrowth. Using the reconstructed model as basis, we generated models with different porosities by varying the amount of quartz cement overgrowth. The value of the cement growth exponent α was 0.6 for all the models.

The predicted permeability versus porosity trend is compared with the experimental data of Bourbie and Zinszer[57] in **Fig 11**. Although the measured permeabilities span nearly five orders of magnitude, the predicted permeability versus porosity trend is in good agreement with the experimental one. **Fig 11** shows that there is a change in the permeability versus porosity trend at approximately 10 to 13% porosity. Our simulation results show that this corresponds to the porosity at which quartz cement begins to close off pore throats. This increases the tortuosity of the medium and the permeability declines more rapidly. **Fig 12** compares predicted and measured[58,59] formation factors. The predicted formation factors are also in good agreement with the measured ones, except for some deviations at high porosities where we tend to underestimate the formation factor. These results demonstrate that our sandstone models and their network representations adequately predict single phase transport properties for this texturally and diagentically simple quartz sandstone.

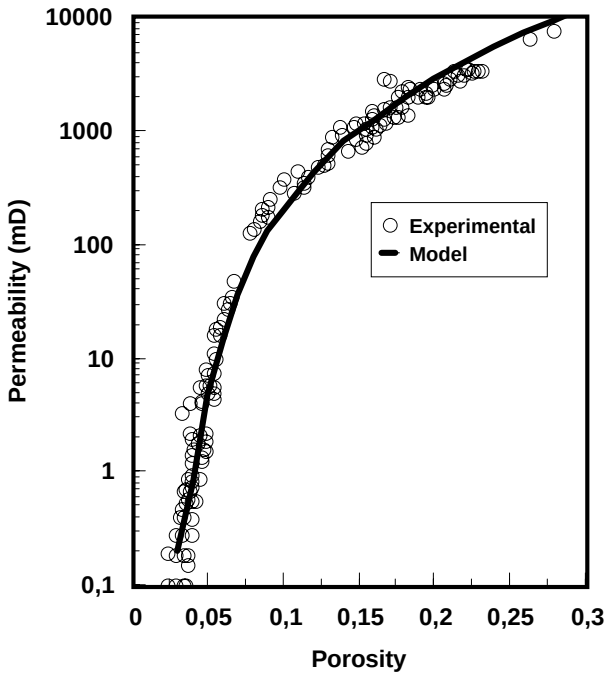

Fig. 11—Comparison between predicted and measured absolute permeability for Fontainebleau sandstone.

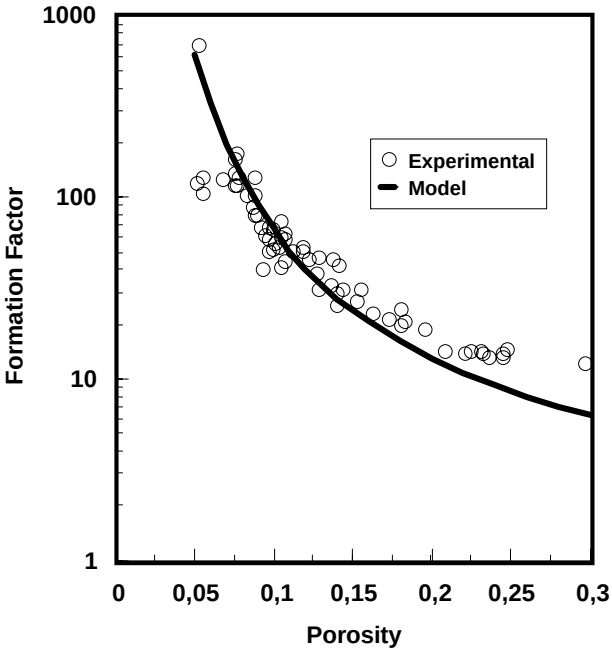

Fig. 12—Comparison between predicted and measured formation factors for Fontainebleau sandstone.

Bentheimer Sandstone. Thin section images of the Bentheimer core plugs described earlier were analysed and used to reconstruct two realisations of each sample. The main input parameters for the reconstruction algorithm are summarised in **Table 5**. Simulated petrophysical properties for the reconstructed samples are compared with measured values in **Table 6**.

TABLE 5—INPUT PARAMETERS FOR THE SANDSTONE RECONSTRUCTION ALGORITHM

Parameter	B1	B2	B3	R1	R2
grain radius (μm)	90-303	90-303	90-303	21-74	21-74
clay content (wt%)	2.5	2.5	2.5	20.0	19.0
clay texture	m	m	m	p-f	p-f
compaction factor	0.05	0.05	0.05	0.0	0.0
cement exponent	-0.2	-0.2	-0.2	1.0	1.0
intergranular porosity	0.194	0.204	0.201	0.210	0.218
size (mm^3)	2.55	2.55	2.55	1.02	1.02
resolution (μm)	10.0	10.0	10.0	4.0	4.0

m = mixture
p-f = pore-filling

TABLE 6—COMPARISON BETWEEN PREDICTED AND MEASURED PETROPHYSICAL PROPERTIES FOR BENTHEIMER (B) AND RESERVOIR (R) ROCK SAMPLES

	Porosity		Permeability (mD)		Form. Factor	
Sample	Exp.	Pred.	Exp.	Pred.	Exp.	Pred.
B1	0.232	0.210	2840	3650	11.6	9.4
B2	0.241	0.219	2820	3906	12.1	11.2
B3	0.237	0.216	2930	3764	12.0	11.1
R1	0.297	0.243	358	429		18.6
R2	0.293	0.245	326	472		17.7

The predicted porosities are 2-3 porosity units less than the plug porosities which were measured with a Helium porosimeter. The discrepancy between measured and predicted porosity is most likely due to differences in the amount of microporosity which is difficult to determine accurately from thin section analyses. Predicted formation factors are in good agreement with the experimental data whilst the predicted permeabilities are approximately 30% higher than the measured ones. This suggests that we overestimate the hydraulic conductance of pore bodies and throats. One possible explanation for this may be that surface roughness is not accounted for in our expression (Eq. (18)) for the hydraulic conductance.

Primary drainage and waterflood displacements were simulated on each of the realisations. In all the simulations the receding contact angle was zero whilst the advancing contact angle for oil invaded pore bodies and throats was randomly distributed between 30^o and 50^o. This is in agreement with contact angle measurements on quartz[60]. The corner resistance factor C_w was calculated assuming a no flow boundary condition at the oil-water interface[56].

Fig. 13 compares simulated and measured drainage capillary pressures. The calculated capillary pressures are the average for the six realisations. The predicted capillary pressure curve is in good agreement with the measured data and we correctly predict the threshold displacement pressure and the low connate water saturation. For the high capillary pressures established at the end of the primary drainage simulations, oil has invaded almost all of the intergranular pore space. The connate water saturation is thus mainly made up of water present in the corners of oil invaded pore bodies and throats and water present in the microporosity which is assumed to be impermeable.

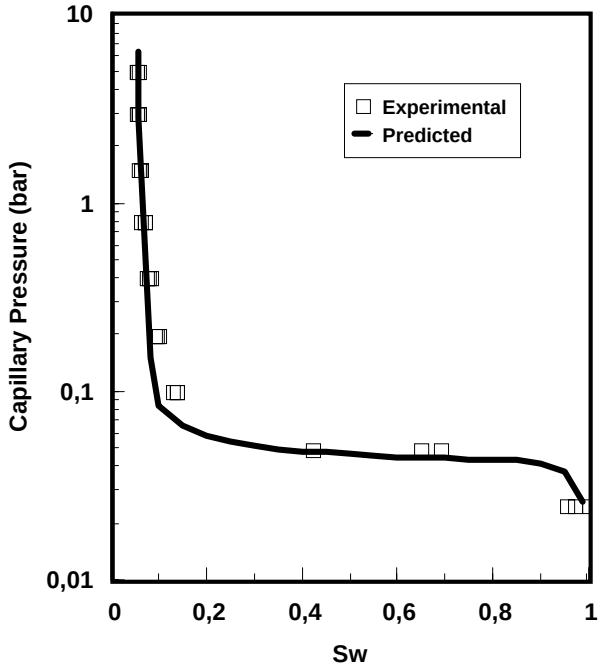

Fig. 13—Comparison between predicted and measured primary drainage capillary pressure for the water wet Bentheimer sandstone.

Simulated primary drainage and waterflood relative permeability curves are compared with experimental data in **Fig. 14**. Although the predicted results are the average of only six realisations, the comparison shows that the network model reproduces the experimental characteristics of the measured data and correctly predicts the waterflood residual oil saturation. At low water saturations, the predicted water permeability is larger than the measured one. This suggest that we overestimate the water conductance in the corners of oil invaded pore bodies and throats. The expression for the corner water conductance (Eq. (19)) assumes a perfectly sharp corner with smooth pore walls. In reality, the pore walls are irregular and rough and their curvature is not zero. Both surface roughness and pore wall curvature can reduce the water conductance

Reservoir Rock. The main clay component in the reservoir rock samples is pore-filling kaolinite. In addition, the samples contain lesser amounts of clay pseudomorphs after K-feldspar, carbonate cement, pyrite, and trace amounts of chlorite. For simplicity, we model all of this as pore-filling clay or cement. Input parameters for the reconstruction algorithm are given in **Table 5**. Two realisations of each core plug were reconstructed. The predicted porosities and permeabilities are given in **Table 6**.

The predicted porosities are about five porosity units less than the Helium porosities. This may be because we underestimate the amount of microporosity or because the thin sections are not fully representative of the core plugs (*i.e.*, heterogeneity). The predicted permeabilities are in fair agreement with the measured values.

As mentioned before, the reservoir rock samples display a mixed wettability. Unfortunately, it is not possible to know *a priori* what fraction of the pore space which is mixed wet nor the contact angles which should be assigned to the water wet

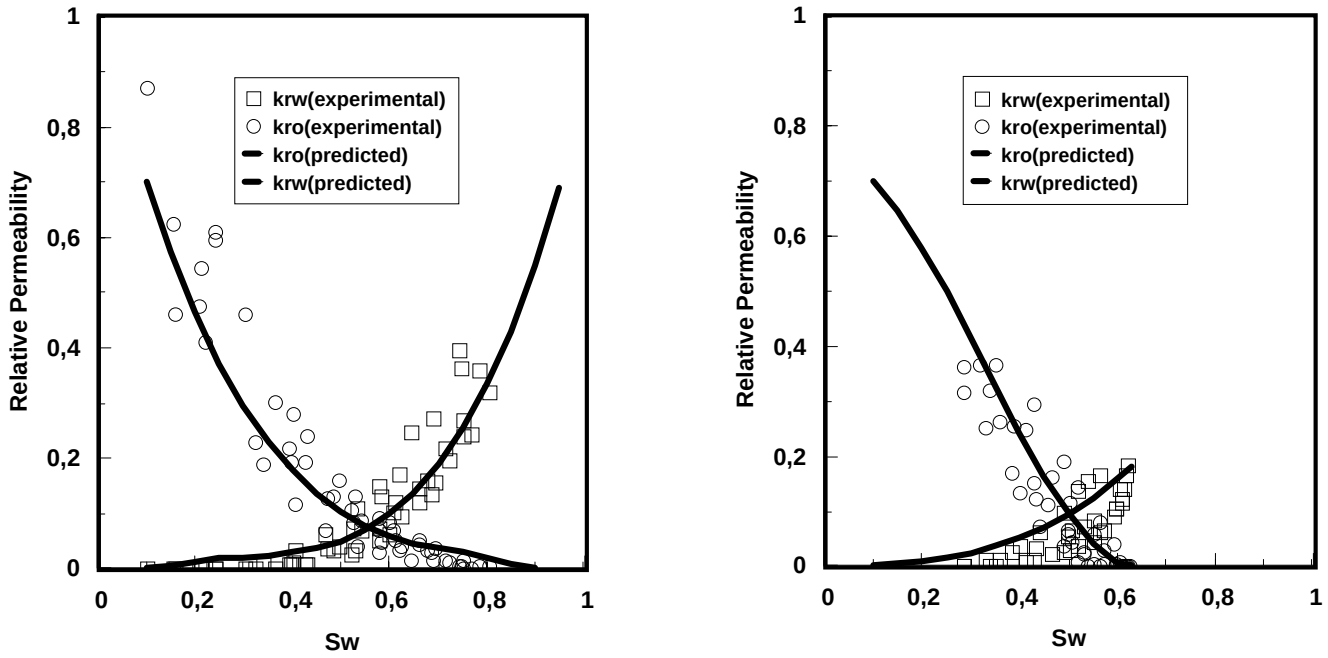

Fig. 14—Comparison between predicted and measured drainage (left) and waterflood (right) relative permeabilities for a water wet Bentheimer sandstone.

and mixed wet regions of the pore space. Instead, we investigate how the waterflood residual oil saturation S_{or} depends on the fraction f of oil invaded pore bodies and throats which become mixed wet.

Fig. 15 shows how S_{or} depends on the fraction of mixed wet pore bodies and throats. In all the simulations, the advancing contact angle for mixed wet pore bodies and throats is 180^o whilst θ_a for the water wet regions is 40^o. The receding angle is 20^o. For small f, the mixed wet regions of the pore space do not form a continuos cluster. Oil is thus trapped in the mixed wet regions of the pore space and S_{or} increases almost linearly with f. At a critical f (around 0.62), mixed wet pore bodies and throats first form a continuous flow path to the outlet. Forced water injection can then displace oil and S_{or} drops sharply. These results are in qualitative agreement with those reported by Blunt[32].

The experimentally determined S_{or} for the reservoir rock is 5%. From **Fig. 15** this corresponds to f = 0.85. Predicted waterflood capillary pressure and relative permeability curves for this case are shown in **Fig. 16**. The simulated capillary pressure curve is in fair agreement with the experimental data except at low oil saturations. At low oil saturations, the simulated capillary pressure curve displays a sharper break than the experimental data. This suggests that the reconstructed sample has a narrower pore size distribution than the actual sample and that some of the smaller pores are not included in the model. In order to capture the presence of these small pores, the resolution of the reconstructed model must be increased. This, however, can only be done at considerable computational expense.

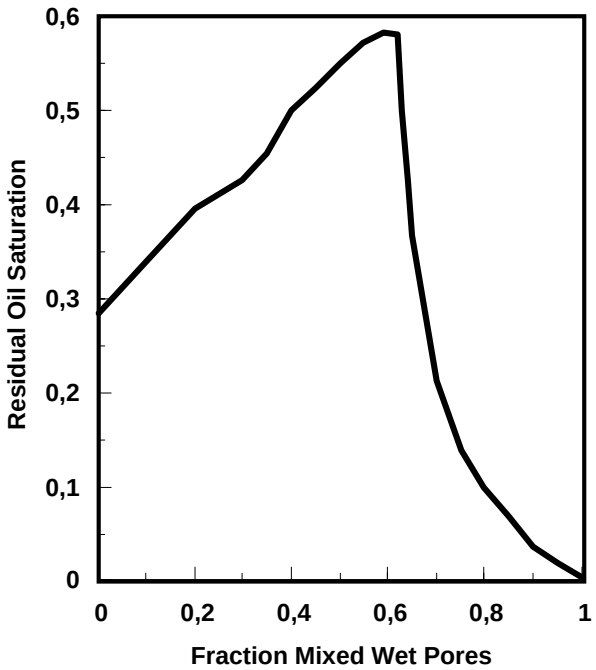

Fig. 15—Waterflood residual oil saturation for the reconstructed reservoir rock as a function of the fraction of pore bodies and throats contacted by oil which become mixed wet.

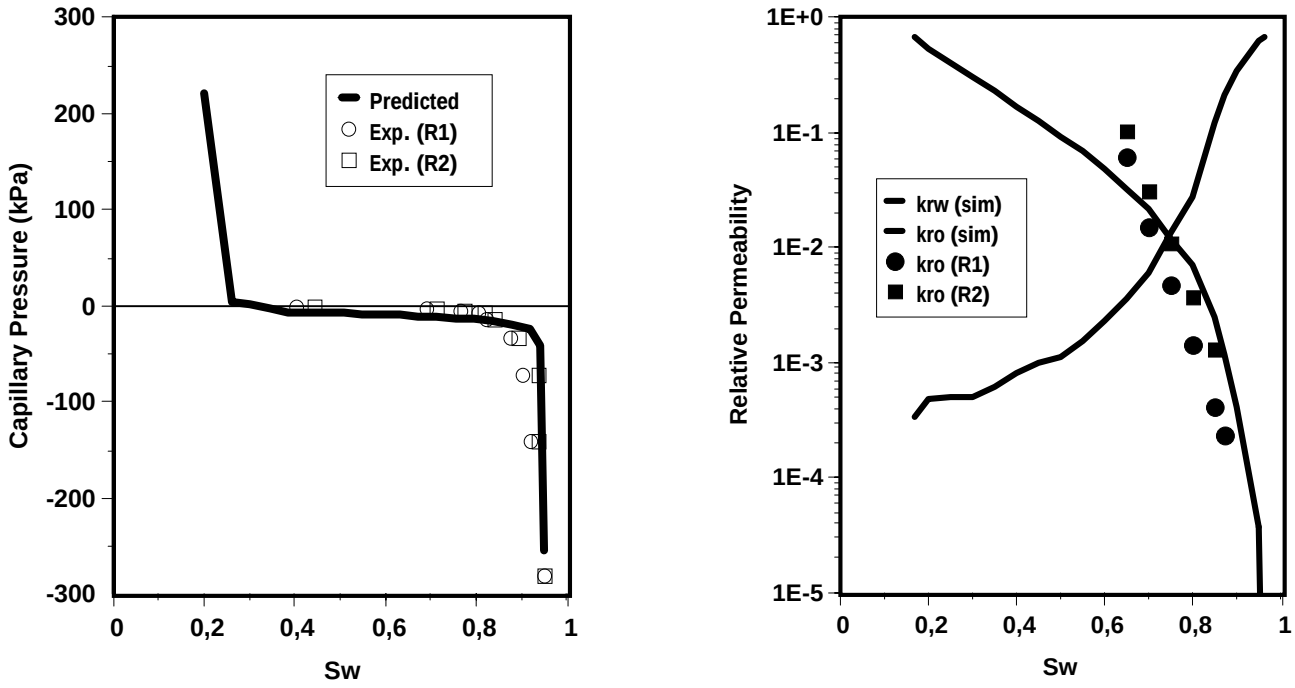

Fig. 16—Comparison between simulated and measured waterflood capillary pressures and relative permeabilities for a mixed wet reservoir rock.

The agreement between the predicted and measured oil relative permeabilities is encouraging. In spite of the necessarily approximate nature for the distribution of water wet and mixed wet pores as well as the uncertain estimates for both the contact angles and the oil film conductance, the predicted and measured oil relative permeability curves display the same generic behaviour. Both the experiments and the simulations show that continuos oil films allow low oil saturations to be reached during forced water injection. However, the oil relative permeability is very low.

The fair agreement between the predicted and measured transport properties for the three different reconstructed sandstones is encouraging. Although we need to examine a much larger group of petrographically and petrophysically heterogeneous rock samples, these preliminary results cautiously suggest that network modeling techniques may be used to *a priori* predict single and multiphase transport properties for real rocks.

Conclusions

1. Petrographical data obtained from image analysis of two-dimensional thin sections are used to reconstruct model sandstones which give a realistic description of the complex microstructure exhibited in real sandstones.

2. Image analysis techniques are used to transform the reconstructed pore space into a pore network which can be used as input to a network simulator.

3. Predicted permeabilities and formation factors of a reconstructed Fontainebleau sandstone model correspond well with published data over a wide range of porosity.

4. Predicted primary drainage and waterflood relative permeability curves for a water wet Bentheimer sandstone are in good agreement with experimental data.

5. Simulated waterflood capillary pressures and oil relative permeabilities for a mixed wet reservoir rock are in fair agreement with experimental measurements.

Nomenclature

A = cross-sectional area
a = parameter controlling the amount of cement growth
b = input parameter, Eq. (9)
C = corner resistance factor
FRF = formation factor
f = fraction of mixed wet pore bodies and throats
G = pore body or throat shape factor
g = conductance
k = permeability
k_r = relative permeability
L = length
L_b = distance between pinned contact line and corner
l = distance between surface of grain and its Voronoi polyhedron
P = pressure
P_c = capillary pressure
P_c^* = threshold capillary pressure for water film collapse, Eq. (6)
$P_{c,max}$ = maximum capillary pressure reached during primary drainage
q = volumetric flowrate
R_n = radius of curvature for pore body filling
r = radius
S_{or} = residual oil saturation
s = perimeter length

u = dimensionless velocity
v = velocity
α = cement growth exponent
β = corner half angle
Γ = input parameter, Eq. (6)
ϕ = porosity
γ = interfacial tension
μ = viscosity
Π = parameter controling water film collapse
θ = contact angle
ρ = density
σ = electrical conductivity

Subscripts

a = advancing
d = drainage
e = electrical
eff = effective
h = hinging
min = minimum
max = maximum
o = oil
p = pore body
pd = primary drainage
pt = piston type
s = solid
r = receding
t = pore throat
w = water

Superscripts

e = entry
d = drainage
N = normalised

Acknowledgments

The authors would like to acknowledge Den norske stats oljeselskap a.s. (Statoil) for granting permission to publish this paper. We are indebted to Svein H. Midtlyng for performing the experimental work. We also graciously thank David Stern, Exxon Research Production Company, for providing us with the microtomography data.

References

1. Fatt, I.: “The Network Model of Porous Media I. Capillary Pressure Characteristics,” *Trans. AIME* (1956), **207**, 144.
2. Fatt, I.: "The Network Model of Porous Media II. Dynamic Properties of a Single Size Tube Network," *Trans. AIME*, (1956), **207**, 160.
3. Fatt, I.: "The Network Model of Porous Media III. Dynamic Properties of Networks with Tube Radius Distribution," *Trans. AIME*, (1956), **207**, 164.
4. Larson, R.G., Scriven, L.E., and Davis, H.T.: "Percolation Theory of Two-Phase Flow in Porous Media", *Chem. Eng. Sci.*, (1981), **36,** 57.
5. Koplik, J.: "Creeping Flow in Two-Dimensional Networks", *J. of Fluid Mechanics.*, (1982), **119**, 219.
6. Koplik, J. and Lasseter, T.J.: "Two-Phase Flow in Random Network Models of Porous Media", *SPEJ*, (1985), **22**, 89.
7. Chan, D.Y.C., Hughes, B.D., Paterson, L., and Sirakoff, C.: "Simulating Flow in Porous Media", *Physical Review A*, (1988), **38**, 4106.
8. Touboul, E., Lenormand, R., and Zarcone, C.: “Immiscible Displacements in Porous Media: Testing Network Models by Micromodel Experiments”, SPE 16954, presented at the 1987 SPE Annual Technical Conference and Exhibition, Sept. 27-30.
9. Lenormand, R., Touboul, E., and Zarcone, C.: "Numerical Models and Experiments on Immiscible Displacements in Porous Media", *J. Fluid Mechanics*, (1988), **189**, 165.
10. Lenormand, R.: “Flow Through Porous Media: Limits of Fractal Patterns”, *Proc. R. Soc. Lond. A*, (1989), **423**, 159.
11. Blunt, M.J. and King, P.R.: "Macroscopic Parameters from Simulation of Pore Scale Flow," *Phys. Rev. A*, (1990), **42**, 4780.
12. Jerauld, G.R. and Salter, S.J.: "The Effect of Pore-Structure on Hysteresis in Relative Permeability and Capillary Pressure: Pore-Level Modelling", *Transport in Porous Media*, (1990), **5**, 103.
13. Blunt, M.J. and King, P.R.: "Relative Permeabilities from Two- and Three-Dimensional Pore-Scale Network Modelling", *Transport in Porous Media*, (1991), **6**, 407.
14. Blunt, M.J., King, M., and Scher, H.: "Simulation and Theory of Two-Phase Flow in Porous Media", *Phys. Rev. A*, (1992), **46**, 7680.
15. Bryant, S. and Blunt, M.J.: "Prediction of Relative Permeability in Simple Porous Media", *Phys. Rev. A*, (1992), **46**, 2004.
16. Bryant, S., King, P.R., and Mellor, D.W.: "Network Model Evaluation of Permeability and Spatial Correlation in a Real Random Sphere Packing", *Transport in Porous Media*, (1993), **11**, 53.
17. Billiotte, J., De Moegen, H., and Øren, P.E.: "Experimental Micromodelling and Numerical Simulation of Gas-Water Injection-Withdrawal Cycles as Applied to Underground Gas Storage", *SPE. Adv. Tech. Ser*., (1993), **1,** 133.
18. McDougall, S.R. and Sorbie, K.S.: "The Combined Effect of Capillary and Viscous Forces on Waterflood Displacement Efficiency in Finely Laminated Porous Media", SPE 26659, presented at the 1993 SPE Annual Technical Conference and Exhibition, Oct. 3-6.
19. Blunt, M.J. and Scher, H.: "Pore Level Modelling of Wetting," *Physical Review E*, (1995), **52**, 6387.
20. Øren, P.E., Bakke, S., Nilsen, L.S., and Henriquez, A.: “Prediction of Relative Permeability and Capillary Pressure from Pore-Scale Modelling”, proceedings of the 1996 European Conference on the Mathematics of Oil Recovery, Leoben, Austria, Sept. 3-6.
21. Hazlett, R.D.: “Simulation of Capillary-Dominated Displacements in Microtomographic Images of Reservoir Rocks”, *Transport in Porous Media*, (1995), **20**, 21.
22. Dunsmoir, J.H., Ferguson, S.R., D’Amico, K.L., and Stokes, J.P.: “X-Ray Microtomography: A New Tool for the Characterization of Porous Media”, SPE 22860, presented at the 1991 SPE Annual Technical Conference and Ehibition, Oct. 6-9.
23. Coles, M.E., Spanne, P., Muegge, E.L., and Jones, K.V.: "Computed Microtomography of Resevoir Core Samples," proceedings of the 1994 International SCA Meeting, Stavanger, Norway, Sept. 12-14.
24. Coles, M.E., Hazlett, R.D., Muegge, E.L., Jones, K.W., Andrews, B., Siddons, P., Peskin, A., and Soll, W.E.: “Developments in Synchroton X-Ray Microtomography with Applications to Flow in Porous Media”, SPE 36531, presented at the 1996 SPE Annual Technical Conference and Exhibition, Oct. 6-9.
25. Baldwin, C.A., Sederman, A.J., Mantle, M.D., Alexander, P., and Gladden, L.F.: “Determination and Characterization of

the Structure of a Pore Space from 3D Volume Images", *J. Colloid and Interface Science*, (1996), **181**, 79.
26. Lin, C. and Cohen, M.H.: "Quantitative Methods of Microgeometric Modelling," *J. Appl. Phys.*, (1982), **53**, 4152.
27. Holt, R., Fjær, E., Torsæter, O., and Bakke, S.: "Petrophysical Laboratory Measurements for Basin and Reservoir Evaluation", *Marine and Petroleum Geology*, (1996), **13**, 383.
28. Dixit, A.B., McDougall, S.R., and Sorbie, K.S.: "A Pore-Level Investigation of Relative Permeability Hysteresis in Water-Wet Systems", SPE 37233, presented at the 1997 SPE International Symposium on Oilfield Chemistry, Feb. 18-21.
29. McDougall, S.R. and Sorbie, K.S.: "The Impact of Wettability on Waterflooding: Pore-Scale Simulation", *SPE Resevoir Engineering*, (1995), **10**, 208.
30. Heiba, A.A., Davis, H.T., and Scriven, L.E.: "Effect of Wettability on Two-Phase Relative Permeabilities and Capillary Pressures", SPE 12172, presented at the 1983 SPE Annual Technical Conference and Exhibition, Oct. 5-8.
31. Blunt, M.J.: "Effects of Heterogeneity and Wetting on Relative Permeability using Pore Level Modelling", *SPEJ*, (1997), **2**, 70.
32. Blunt, M.J.: "Pore Level Modelling of the Effects of Wettability", *SPEJ*, (1997), **2**, 449.
33. Soll, W.E. and Celia, M.A.: "A Modified Percolation Approach to Simulating Three-Fluid Capillary Pressure-Saturation Relationships", *Advances in Water Resources*, (1993), **16**, 107.
34. Øren, P.E., Billiotte, J., and Pinczewski, W.V.: "Pore-Scale Network Modelling of Waterflood Residual Oil Recovery by Immiscible Gas Flooding", SPE 27814, presented at the 1994 SPE/DOE 9th Symposium on IOR, April 17-20.
35. Øren, P.E. and Pinczewski, W.V.: "Fluid Distribution and Pore-Scale Displacement Mechanisms in Drainage Dominated Three-Phase Flow", *Transport in Porous Media*, (1995), **20**, 105.
36. Fenwick, D.H. and Blunt, M.J.: "Pore Level Modelling of Three Phase Flow in Porous Media", proceedings of the 1995 European IOR Symposium, Vienna, Austria, May 15-17.
37. Pereira, G.G., Pinczewski, W.V, Chan, D.Y.C., Paterson, L., and Øren, P.E.: "Pore-Scale Network Model for Drainage Dominated Three-Phase Flow in Porous Media", *Transport in Porous Media*, (1996), **24**, 167.
38. Mani, V. and Mohanty, K.K.: "Effect of the Spreading Coefficient on Three-Phase Flow in Porous Media", *J. Colloid and Interface Science*, (1997), **187**, 45.
39. Hagoort, J.: "Oil Recovery by Gravity Drainage", *SPEJ*, (1980), **20**, 139.
40. Bakke, S. and Øren, P.E.: "3-D Pore-Scale Modelling of Sandstones and Flow Simulations in the Pore Networks", *SPEJ*, (1997), **2**, 136.
41. Schwartz, L.M. and Kimminau, S.: "Analysis of Electrical Conduction in the Grain Consolidation Model", *Geophysics*, (1987), **52**, 1402.
42. Roberts, J.N. and Schwartz, L.M.: "Grain Consolidation and Electrical Conductivity in Porous Media", *Physical Review*, (1985), **B31**, 5990.
43. Adler, P.M., Jacquin, C.G., and Quiblier, J.A.: "Flow in Simulated Porous Media", *Int. J. Multiphase Flow*, (1990), **16**, 691.
44. Adler, P.M., Jacquin, C.G., and Thovert, J.F.: "The Formation Factor of Reconstructed Porous Media", *Water Resources Research*, (1992), **28**, 1571.
45. Ferreol, B. and Rothman, D.H.: "Lattice-Boltzmann Simulations of Flow through Fontainebleau Sandstone", *Transport in Porous Media*, (1995), **20**, 3.
46. Mason, G. and Morrow, N.R.: "Capillary Behaviour of a Perfectly Wetting Liquid in Irregular Triangular Tubes", *J. of Colloid and Interface Science*, (1991), **141**, 262.
47. Hilfer, R. and Øren, P.E.: "Dimensional Analysis of Pore Scale and Field Scale Immiscible Displacement", *Transport in Porous Media*, (1996), **22**, 53.
48. Wilkinson, D. and Willemsen, J.F.: "Invasion Percolation: A New Form of Percolation Theory", *J. of Physics A*, (1983), **16**, 3365.
49. Chandler, R., Koplik, J., Lerman, K., and Willemsen, J.F.: "Capillary Displacement and Percolation in Porous Media", *J of Fluid Mechanics*, (1982), **119**, 249.
50. Mayer, R.P. and Stowe, R.A.: "Mercury Porosimetry-Breakthrough Pressure for Penetration between Packed Spheres", *J. Colloid and Interface Science*, (1965), **20**, 893.
51. Princen, H.M.: "Capillary Phenomena in Assemblies of Parallel Cylinders I. Capillary Rise between Two Cylinders", *J. Colloid and Interface Science*, (1969), **30**, 60.
52. Princen, H.M.: "Capillary Phenomena in Assemblies of Parallel Cylinders II. Capillary Rise in Systems with More Than Two Cylinders", *J. Colloid and Interface Science*, (1969), **30**, 359.
53. Princen, H.M.: "Capillary Phenomena in Assemblies of Parallel Cylinders III. Liquid Columns between Horizontal Parallel Cylinders", *J. Colloid and Interface Science*, (1970), **34**, 171.
54. Kovscek, A.R., Wong, H., and Radke, C.J.: "A Pore-Level Scenario for the Devlopment of Mixed Wettability in Oil Reservoirs", *AIChE J*., (1993), **39**, 1072.
55. Lenormand, R., Zarcone, C., and Sarr, A.: "Mechanism of the Displacement of One Fluid by Another in a Network of Capillary Ducts", J. Fluid Mechanics, (1983), **135**, 337.
56. Ranshoff, T.C. and Radke, C.J.: "Laminar Flow of Wetting Liquid along the Corners of a Predominantly Gas-Occupied Noncircular Pore", *J. of Colloid and Interface Science*, (1988), **121**, 392-401.
57. Bourbie, T. and Zinszner, B.: "Hydraulic and Acoustic Properties as a Function of Porosity in Fontainebleau Sandstone", *J. of Geophysical Research*, (1985), **90**, 11524.
58. Jacquin, C.G.: " Correlation entre la Permeabilite et les Caracteristiques Geometriques du gres de Fontainebleau", *Rev. Inst. Fr. Pet.*, (1964), **19**, 921.
59. Fredrichs, J.T., Greaves, K.H., and Martin, J.W.: "Pore Geometry and Transport Properties of Fonatainebleau Sandstone", *Int. J. Rock Mech. Min. Sci. & Geomech*., (1993), **30**, 691.
60. Hjelmeland, O., Selle, O.M., and Rueslåtten, H.: "The Effects of Rock Properties on Wettability of Oil Reservoirs - An Investigation of North Sea Systems", Proceeding of the 1987 European Symposium on Enhanced Oil Recovery, Hamburg, Germany, Oct. 27-29.
61. Morrow, N.R.: "Pore Level Displacement Mechanisms", presented at the 1st International. Symposium on Evaluation of Reseservoir Wettability and Its Effect on Oil Recovery, Socorro, NM, Sept. 18-21, 1990.
62. Ma, S., Mason, G., and Morrow, N.R.: "Effect of Contact Angle on Drainage and Imbibition in Regular Polygonal Tubes", *Colloids and Surfaces A*, (1996), **117**, 273.

Appendix A - Threshold Pressures

Mason and Morrow[46] applied the MS-P method to derive a general expression in terms of G for the drainage threshold capillary pressure in strongly wetted triangular pores. This analysis was later extended to include the effect of contact angle and contact angle hysteresis in equilateral triangular pores[61]. In the present work, we generalise this model to any

shape triangular pores. Our computations are similar to those reported by Ma *et al.*[62] for the displacement curvature of a meniscus in regular polygonal tubes.

Drainage. Capillary forces prevent oil from spontaneously entering water filled throats. Oil can only enter an available throat if the capillary pressure exceeds the threshold capillary pressure. At the threshold capillary pressure, oil enters the throat with a fixed curvature and displaces water from the central part of the throat, leaving some of the water as arc menisci (AMs) in the corners. In the absence of gravity, the curvature of these AMs is the same as the curvature of the invading interface.

The MS-P method for calculating threshold capillary pressures relies on equating the curvature, $1/r_d$, of the AMs to the curvature of the invading interface. If the AMs are displaced a small distance dx, the work of the displacement must be balanced by the change in surface free energy

$$P_c A_{eff}\, dx = (L_{ow}\gamma_{ow} + L_{os}\gamma_{os} - L_{os}\gamma_{ws})dx \qquad \text{(A-1)}$$

where the subscript s denotes the solid, A_{eff} is the effective area occupied by oil, L_{os} is the length of the solid wall in contact with oil, and L_{ow} is the perimeter length of the AMs. From Young's equation, γ_{os} - γ_{ws} = $\gamma_{ow}\cos\theta_r$ and Eq. (A-1) simplifies to

$$\frac{P_c}{\gamma_{ow}} = \frac{1}{r_d} = \frac{L_{ow} + L_{os}\cos\theta_r}{A_{eff}} = \frac{L_{eff}}{A_{eff}} \qquad \text{(A-2)}$$

The curvature of the invading interface at the condition for invasion is thus given as the ratio of the effective perimeter to the effective area. A_{eff}, L_{ow}, and L_{os} are readily determined from elementary geometry and are given by

$$A_{eff} = A - r_d^2 \sum_{i=1}^{3}\left[\frac{\cos\theta_r\cos(\theta_r+\beta_i)}{\sin\beta_i} - \frac{\pi}{2}\left(1 - \frac{\theta_r+\beta_i}{90}\right)\right] = \frac{r^2}{4G} - r_d^2 S_1 \qquad \text{(A - 3)}$$

$$L_{os} = \frac{r}{2G} - 2r_d\sum_{i=1}^{3}\frac{\cos(\theta_r+\beta_i)}{\sin\beta_i} = \frac{r}{2G} - 2r_d S_2 \qquad \text{(A-4)}$$

$$L_{ow} = \frac{2\pi r_d}{180}\sum_{i=1}^{3}(90 - \theta_r - \beta_i) = r_d S_3 \qquad \text{(A-5)}$$

After a bit of algebra, we obtain a quadratic expression for r_d which has the solution

$$r_d = \frac{r\cos\theta_r(-1 \pm \sqrt{1 + 4GD/\cos^2\theta_r})}{4GD} \qquad \text{(A-6)}$$

where $D = S_1 - 2S_2\cos\theta_r + S_3$. The radius of curvature r_d is given by the valid root (smaller radius than the inscribed radius r) of Eq. (A-6) and may be expressed as

$$\frac{r}{r_d} = P_c\frac{r}{\gamma_{ow}} = \cos\theta_r(1 + 2\sqrt{\pi G})F_d(\theta_r, G) \qquad \text{(A-7)}$$

where the function $F_d(\theta_r,G)$ is given by

$$F_d(\theta_r, G) = \frac{1 + \sqrt{1 + 4GD/\cos^2\theta_r}}{1 + 2\sqrt{\pi G}} \qquad \text{(A-8)}$$

In general, $F_d(\theta_r,G)$ is dependent on the particular corner angles and is not universal for a specific G. However, if AMs are present in all the corners, the expression for D becomes

$$D = \pi\left(1 - \frac{\theta_r}{60}\right) + 3\sin\theta_r\cos\theta_r - \frac{\cos^2\theta_r}{4G} \qquad \text{(A-9)}$$

D is thus only dependent on θ_r and $F_d(\theta_r,G)$ is universal for a particular G.

Piston Type. If there is contact angle hysteresis, the threshold capillary pressure for piston type invasion during water injection is different from that during drainage. The invading interface enters the throat once the curvature is lowered sufficiently that θ_a is reached. The oil-water interfaces of the AMs in the throat remain pinned at the position L_b established at the end of the primary drainage, *i.e.*,

$$L_{bi} = r_{pd}\frac{\cos(\theta_r + \beta_i)}{\sin\beta_i} \qquad \text{(A-10)}$$

where $r_{pd} = \gamma/P_{c,max}$ and L_{bi} is the distance between the pinned contact line and the corner i. As the capillary pressure drops, the hinging angle of the pinned AMs adjusts to give the same curvature as for the invading interface. Provided that θ_a is not too large, the invading interface meets these AMs at zero contact angle. The radius of curvature r_{pt} of the AMs may be calculated by equating r_{pt} to A_{eff}/L_{eff}. The effective area A_{eff} is given by Eq. (A-3), but with r_{pt} substituted for r_d and θ_r replaced by the hinging angle $\theta_{h,i}$

$$\theta_{h,i} = \cos^{-1}\left(\frac{r_{pd}}{r_{pt}}\cos(\theta_r + \beta_i)\right) - \beta_i \qquad \text{(A-11)}$$

The effective perimeter P_{eff} is given by

$$L_{eff} = \cos\theta_a\left(\frac{r^2}{2G} - 2\sum_{i=1}^{3}L_{bi}\right) + \frac{2\pi r_{pt}}{180}\sum_{i=1}^{3}\alpha_i \qquad \text{(A-12)}$$

where the angle α_i is given by

$$\alpha_i = \sin^{-1}\left(\frac{L_{bi}\sin\beta_i}{r_{pt}}\right) \qquad \text{(A-13)}$$

The above equations constitute a non-linear system of equations which can be solved numerically for the radius of curvature r_{pt} and thus the threshold capillary pressure $P_c = \gamma/r_{pt}$. The maximum advancing angle at which spontaneous imbibition occurs is given by Eq. (7) and corresponds to the limit when $L_{eff} = 0$. If $\theta_a > \theta_{a,max}$, the threshold capillary pressure may be determined from Eqs. (5) or (8).

Snap-Off. If $\theta_a < 90^o - \beta_1$, snap-off occurs when the advancing AM in the sharpest corner meets one of the other AMs. For small values of θ_a, all the AMs advance towards the centre of the pore space at θ_a and snap-off occurs when the AMs in the two sharpest corners meet. This occurs at a threshold capillary pressure

$$P_c = \frac{\gamma}{r}\left(\cos\theta_a - \frac{2\sin\theta_a}{\cot\beta_1 + \cot\beta_2}\right) \qquad \text{(A-14)}$$

For larger values of θ_a, the AM in the largest corner may remain pinned whilst the two other AMs advance at θ_a. Snap-off then occurs either when the two advancing AMs meet or when the AM in the sharpest corner meets the pinned AM. The threshold capillary pressure for the first case is given by Eq. (A-14) whilst the threshold capillary pressure in the second case is

$$P_c = \frac{\gamma}{r}\left(\frac{\cos\theta_a \cot\beta_1 - \sin\theta_a + \cos\theta_{h3}\cot\beta_3 - \sin\theta_{h3}}{\cot\beta_1 + \cot\beta_3}\right) \qquad \text{(A-15)}$$

The event which actually takes place is the one occurring at the highest capillary pressure. Because the hinging angle depends on the prevailing capillary pressure, the above equation can not be solved analytically. If $\theta_a > 90^o - \beta_1$, the curvatures of the AMs are negative and the threshold capillary pressure is given by Eq. (10) or (11).

SI Metric Conversion Factors

cp	x 1.0*	E–03	= Pa. s
md	x 9.869223	E–04	= μm^2

*Conversion factor is exact

SPEJ

Pål-Eric Øren, SPE, is a research scientist at Statoil Research Centre, Postuttak, N-7005 Trondheim, Norway, email: peoe@statoil.com. His research interests include physics of multiphase flow in porous media and reservoir engineering. Øren holds a BS in chemical engineering from the University of Michigan, and a PhD in petroleum engineering from the University of New South Wales. **Stig Bakke** is a geologist at Statoil Research Centre, Postuttak, N-7005 Trondheim, Norway, email: stiba@statoil.com. His research interests include micro-scale reservoir description, numerical modeling of geological process, and 2-D and 3-D image analysis. Before joining Statoil, he worked at IKU, Trondheim. Bakke holds a MS in geology from NTH. **Ole Jakob Arntzen** is a research scientist at Statoil Research Centre, Postuttak, N-7005 Trondheim, Norway, email: oja@statoil.com. His research interests include multiphase flow in porous media, probability and statistics. Arntzen holds a MS in applied mathematics. Before joining Statoil he worked at the Norwegian Defense Research Establishment.